Science
AAAS

Supplementary Materials for

A nearby transiting rocky exoplanet that is suitable for atmospheric investigation

T. Trifonov, J. A. Caballero, J. C. Morales, A. Seifahrt, I. Ribas, A. Reiners, J. L. Bean, R. Luque, H. Parviainen, E. Pallé, S. Stock, M. Zechmeister, P. J. Amado, G. Anglada-Escudé, M. Azzaro, T. Barclay, V. J. S. Béjar, P. Bluhm, N. Casasayas-Barris, C. Cifuentes, K. A. Collins, K. I. Collins, M. Cortés-Contreras, J. de Leon, S. Dreizler, C. D. Dressing, E. Esparza-Borges, N. Espinoza, M. Fausnaugh, A. Fukui, A. P. Hatzes, C. Hellier, Th. Henning, C. E. Henze, E. Herrero, S. V. Jeffers, J. M. Jenkins, E. L. N. Jensen, A. Kaminski, D. Kasper, D. Kossakowski, M. Kürster, M. Lafarga, D. W. Latham, A. W. Mann, K. Molaverdikhani, D. Montes, B. T. Montet, F. Murgas, N. Narita, M. Oshagh, V. M. Passegger, D. Pollacco, S. N. Quinn, A. Quirrenbach, G. R. Ricker, C. Rodríguez López, J. Sanz-Forcada, R. P. Schwarz, A. Schweitzer, S. Seager, A. Shporer, M. Stangret, J. Stürmer, T. G. Tan, P. Tenenbaum, J. D. Twicken, R. Vanderspek, J. N. Winn

Correspondence to: trifonov@mpia.de

This PDF file includes:

Materials and Methods
Figs. S1 to S10
Tables S1 to S6

Materials and Methods

Spectroscopic observations

Spectroscopic data employed for the RV analysis were obtained with the CARMENES spectrograph, the newly commissioned MAROON-X spectrograph, and from archival data from the High Resolution Echelle Spectrometer (HIRES) (32) at the 10.0 m Keck I Telescope, and the

High Accuracy Radial velocity Planet Searcher (HARPS) (33) at the European Southern Observatory (ESO) 3.6 m Telescope. Fig. S1 shows the available RV data combined after subtraction of the mean RV offset.

Gliese 486 (34) is one of the about 350 M-dwarf targets regularly monitored in the CARMENES (Calar Alto high-Resolution search for M dwarfs with Exo-earths with Near-infrared and optical Echelle Spectrographs) guaranteed time observation program. Detailed descriptions of the CARMENES instrument at the 3.5 m Calar Alto telescope and the on-going exoplanet survey can be found in (*1*) and (10). For Gliese 486 we obtained 80 pairs of optical (VIS: 520-960 nm) and near-infrared (NIR: 960-1710 nm) spectra between January 2016 and June 2020 with a total time baseline of 1612.7 d. The typical exposure time was about 20 min, chosen with the goal of reaching a signal-to-noise ratio (S/N) of 150 in the *J* band. All the spectra went through the standard CARMENES data flow (3*5*). Using the version 2.20 of the data reduction pipeline and of the SpEctrum Radial Velocity AnaLyser (SERVAL) (36), we computed VIS and NIR radial velocity (RV) measurements. Additionally, we computed and corrected the nightly zero-point (NZP) offsets of the CARMENES data (3*7*). Four CARMENES epochs were discarded because the spectra were taken without simultaneous Fabry-Pérot etalon wavelength calibration. The resulting 76 VIS RVs had a weighted root-mean-square velocity, $wrms_{C-VIS}$, of 2.56 m s^{-1} and a median uncertainty, $\hat{\sigma}_{C-VIS}$, of 1.17 m s^{-1}. We additionally discarded 16 NIR spectra obtained before the start of the nominal operations of the NIR channel (3*8*). For the remaining 60 CARMENES NIR measurements of Gliese 486 we measured $wrms_{C-NIR} = 6.36$ m s^{-1} and $\hat{\sigma}_{C-NIR} = 4.36$ m s^{-1}. Simultaneously with the RVs extraction from CARMENES spectra, SERVAL computes the time series of several stellar activity indices: the chromatic index (CRX), the differential line width (dLW), calcium infrared triplet (Ca IRT), Hα, and Na I D1 and D2. Using the RACOON pipeline (39), from the CARMENES spectra we also calculated the full-width half-maximum (FWHM) of the cross-correlation function (CCF) profile, the bisector inverse slope (BIS) span, and contrast stellar line measurement (CON) of the spectral lines (40). The time series of the RV and all activity indices from CARMENES VIS and NIR channels, together with their individual uncertainties, are listed in Tables S1 and S2, respectively.

We also performed RV observations of Gliese 486 using the MAROON-X instrument (20, *41*) on the 8.1 m Gemini North telescope. MAROON-X is a fiber-fed double-channel optical (blue: 500-670 nm, red: 650-920 nm) spectrograph with a resolving power R = 85,000 designed for RV observations of M dwarfs. We obtained 65 spectra of Gliese 486 in 17 visits over 13 nights between 20 May and 02 June 2020 using MAROON-X. Visits comprised between two and six consecutive exposures of 300 or 600 s each, depending on seeing conditions and cloud coverage. The typical S/N per pixel was about 120 and 280 in the blue and red channels, respectively. Each spectral resolution element is sampled by 3.2 pixels on average. The MAROON-X data were reduced using a custom Python 3 pipeline based on tools previously developed for the CRyogenic high-resolution InfraRed Echelle Spectrograph (CRIRES) (*42, 43*). The MAROON-X data reduction software, which is being incorporated into Gemini's data reduction platform, can meanwhile be provided upon reasonable request. Similarly to CARMENES, the MAROON-X wavelength calibration strategy used stabilized Fabry-Pérot etalon exposures that were taken simultaneously with the data using a dedicated fiber. The instrumental drift correction was part of the wavelength calibration. Radial velocities and activity

indices were measured using SERVAL. MAROON-X red data have $\text{wrms}_{\text{MX-red}} = 2.26 \text{ m s}^{-1}$ and $\hat{\sigma}_{\text{MX-red}} = 0.39 \text{ m s}^{-1}$, and blue data have $\text{wrms}_{\text{MX-blue}} = 2.36 \text{ m s}^{-1}$ and $\hat{\sigma}_{\text{MX-blue}} = 0.82 \text{ m s}^{-1}$. The time series of the RV and all activity indices from MAROON-X red and blue, together with their individual uncertainties, are listed in Tables S3 and S4, respectively.

We retrieved archival RV measurements of Gliese 486 taken with HIRES and HARPS. There are 27 HIRES RVs in a published catalogue (44), with later NZP corrections (45). For Gliese 486 these datasets (44) and (45) are almost identical, but we decided to use the corrected data set for consistency with the CARMENES data (37). The HIRES observations of Gliese 486 were taken between January 1998 and January 2011, with a total temporal baseline of 4740.8 d. After removing an obvious outlier at barycentric Julian date BJD = 2452006.986 with a 3σ-clipping filter, the HIRES RV data have a $\text{wrms}_{\text{HIRES}} = 6.64 \text{ m s}^{-1}$ and a $\hat{\sigma}_{\text{HIRES}} = 3.22 \text{ m s}^{-1}$, which are larger than those of CARMENES and MAROON-X. There are 12 NZP-corrected HARPS RVs of Gliese 486 in the HARPS-RVBank database (46). The corresponding spectra were taken between June 2004 and May 2011 with a total temporal baseline of 2533.0 d. The HARPS RV data have $\text{wrms}_{\text{HARPS}} = 3.33 \text{ m s}^{-1}$ and $\hat{\sigma}_{\text{HARPS}} = 1.16 \text{ m s}^{-1}$. HARPS-RVBank also tabulates CRX, dLW, Ca IRT, Hα, and Na I D1 and D2 computed with SERVAL and FWHM, BIS, and CON computed with the Data Reduction Software (DRS), the standard HARPS pipeline.

Photometric monitoring

Gliese 486 (TOI-1827) was observed in 2 min short-cadence integrations by the TESS spacecraft in Sector 23, camera 1, detector chip number 3, between 18 March 2020 and 16 April 2020. We retrieved the TESS data from the Mikulski Archive for Space Telescopes. For this target, the Science Processing Operations Center (SPOC) (47) provided both simple aperture photometry (SAP) and systematics-corrected photometry adapted from the *Kepler* Pre-search Data Conditioning algorithm (PDC) (48, 49). The PDC light curve is constructed by detrending the SAP light curve using a linear combination of cotrending basis vectors, which are derived from a principal component decomposition of the light curves individually for each sector, camera, and CCD. PDC light curves are corrected for contamination from nearby stars and instrumental systematics including pointing drifts, focus changes, and thermal transients. Fig. S2 shows the target pixel file (TPF) image of Gliese 486 constructed from TESS and *Gaia* DR2 data with the TPFPLOTTER tool (50), and a false-color image from *u'*-, *i'*-, *z'*-band Sloan Digital Sky Survey (SDSS9) data (51) with the Aladin sky atlas (52). Comparing Fig. S2 to previous adaptive optics (14) and *Hubble Space Telescope* high-resolution imaging, we expect negligible flux dilution by stellar contaminants in the TESS aperture mask in the epoch of TESS observations (and all photometric observations described below (53)).

We carried out additional ground-based photometric monitoring and retrieved archival magnitude series for ruling out nearby eclipsing binaries, further characterizing the transit events, and trying to determine the stellar rotation period. Three transits of Gliese 486 b were observed simultaneously in *g*, *r*, *i*, and *zs* bands with the Multicolour Simultaneous Camera for studying Atmospheres of Transiting exoplanets 2 (MuSCAT2) (18) on the 1.52 m Telescopio Carlos Sánchez at Observatorio del Teide on 9 May 2020, 12 May 2020, and 3 June 2020. The observations on 9 May covered 1.7 h centred around the expected transit mid-time, with airmass

varying from 1.2 at the beginning of the observations to 1.8 at the end of the observations. The observations on 12 May covered 4.3 h approximately centered around the expected transit mid-time with airmass covering values from 1.05 to 1.45. The observations on 3 June were affected by poor weather conditions, so not used. All MuSCAT2 observations were defocused, optimizing the photometry for a star as bright as Gliese 486. However, the lack of suitably bright comparison stars in the field of view led to a sub-optimal photometry, and the white noise estimates in the reduced light curves vary from ~ 2.3 ‰ in *g* to ~ 1.6 ‰ in *zs*. We performed relative photometry using standard aperture photometry calibration and reduction steps with a dedicated MuSCAT2 photometry pipeline based on PYTRANSIT (*54, 55*). The pipeline calculates aperture photometry for a set of comparison stars and aperture sizes, and produces the final relative light curves via global optimization of a model that aims to find the optimal comparison stars and their aperture size while simultaneously modeling the transit and baseline variations as linear combinations of a set of covariates.

We observed three full transits of Gliese 486 with Las Cumbres Observatory Global Telescope (LCOGT) 1.0 m network (*19*) in the *z* filter on 15 May 2020, 24 May 2020, and 5 June 2020. The telescopes are equipped with 4k × 4k cameras having an image scale of 0.389 arcsec pixel[-1], resulting in a 26 × 26 arcmin[2] field of view. The telescopes were defocused and yielded point spread functions with FWHM of approximately 8 arcsec. The transits on 15 May 2020 and 24 May 2020 were observed continuously for 235 and 187 min from the LCOGT node at the South African Astronomical Observatory using 25 s exposures, which resulted in 240 and 171 images, respectively. The transit on 5 June 2020 was observed continuously for 247 min from the LCOGT node at Siding Spring Observatory using 25 s exposures, which resulted in 251 images. The images were calibrated by the standard LCOGT *BANZAI* pipeline (*56*) and the photometric data were extracted using the ASTROIMAGEJ software package (*57*). Circular apertures with radius 25, 30, and 20 pixels were used to extract differential photometry from the 15 May 2020, 24 May 2020, and 5 June 2020 data, resulting in model residuals of 660, 350, 380 ppm in 10 min bins, respectively.

We observed a full transit of Gliese 486 b continuously for 258 min on 08 Jun 2020 in *Rc* band with the Perth Exoplanet Survey Telescope (PEST) near Perth, Australia. The 0.3 m telescope is equipped with a 1.5k × 1k camera with an image scale of 1.2 arcsec pixel[-1], resulting in a 31 × 31 arcmin[2] field of view. The images had typical stellar point spread functions with a FWHM of 4.0 arcsec. The data did not detect the transit, but did rule out nearby eclipsing binaries in all six stars within 2.5 arcmin of the target that are bright enough to contaminate the TESS data.

The Wide Angle Search for Planets (WASP) transit search consisted of two wide-field arrays of eight cameras, with SuperWASP-North being at the Observatorio del Roque de Los Muchachos in La Palma, Spain, and WASP-South being at the South African Astronomical Observatory in Sutherland, South Africa (*16*). The field of Gliese 486 was observed by both arrays. SuperWASP-North observed Gliese 486 in four consecutive seasons from 2008 to 2011, for spans between 50 and 120 d each season. It was equipped with a 200 mm f/1.8 lens with a broadband filter spanning 400-700 nm, backed by 2k × 2k CCDs, giving a plate scale of 13.7 arcsec pixel[−1]. Observations on every clear night rastered available fields with a typical 15 min cadence. In 2013 and 2014, Gliese 486 was observed by WASP-South for spans of 120 and 170

d. The array was then equipped with 85 mm f/1.2 lenses with an SDSS *r'* filter, giving a plate scale of 32 arcsec pixel^{-1}. In the magnitude range of Gliese 486, SuperWASP-North, with its bigger lens and finer plate scale, provided less red noise and better background subtraction than WASP-South. In total, we collected over 51 714 SuperWASP photometric measurements of Gliese 486 from the Northern (wrms = 0.012 mag) and Southern (wrms = 0.051 mag) hemispheres. For comparison purposes and monitoring of systematics, we also collected the light curves of four nearby stars with similar brightness. These stars were; 1SWASP J124802.97+094759.9, V=12.95 mag., 1SWASP J124816.33+095108.4, V=12.58 mag., BD+10 2472, V= 9.70 mag., and TYC 882-378-1, V=11.34 mag.

We searched for public time series data of wide-area photometric surveys and databases following (*58*). The sparse All-Sky Automated Survey ASAS (*59*) and Northern Sky Variability Survey NSVS (*60*) data sets of Gliese 486 with rms of 0.066 mag and 0.032 mag, respectively, did not have any significant peak with <0.1% FAP in the periodograms. We also retrieved light curves from the All-Sky Automated Survey for SuperNovae (ASAS-SN) (*61*) in the *g'* and *V* bands, which spanned from November 2012 to May 2020. Because Gliese 486 has a high proper motion, we obtained the *V*- and *g'*-band magnitudes from ASAS-SN by season. We retrieved the calculated real-time magnitudes using aperture photometry centred on the expected equatorial coordinates of Gliese 486 at the middle of every observing season (mid March). The ASAS-SN *V*- and *g'*-band magnitudes are zero-point calibrated with the American Association of Variable Star Observers Photometric All Sky Survey APASS catalogue (62). In total, we retrieved 2175 archival data points, of which 984 were taken in the *V* band (972 useful, wrms = 0.020 mag) and 1191 in the *g'* band (1064 useful, wrms = 0.039 mag).

We conducted observations with the 0.8 m Telescopi Joan Oró (TJO) at the Observatori Astronòmic del Montsec in Lleida, Spain, as part of the CARMENES photometric follow-up program. We aimed to cover the ±3σ phase window around the conjunction time predicted by the RV solution at the time of observations. The transit time 1σ uncertainty of 2.35 hr implied monitoring Gliese 486 over a time window of 7 h at both sides of the predicted zero phase. We collected data on 9, 11, and 14 April, and 3 May 2020, obtaining a total of 1578 images with the Johnson *R* filter using the Large Area Imager for Astronomy (LAIA) imager, a 4k × 4k CCD with a field of view of 30 arcmin and a scale of 0.4 arcsec pixel^{-1}. The images were calibrated with dark, bias, and flat fields frames using the observatory pipeline. Differential photometry was extracted with *AstroImageJ* using the aperture size and the set of comparison stars selected to minimize the rms of the photometry. We covered most of the early side of the foreseen time window, including the predicted transit epoch. However, no transit was detected. The TESS data later showed the transit occured 2.04 h later than we had initially predicted (but within the 1σ uncertainty at that time), corresponding to an orbital phase that had not been sampled.

Stellar parameters and rotation period

Stellar parameter estimates for Gliese 486 are given in Table 1. Published spectral types of Gliese 486 have varied between M3.0 V (*63*) and M4.0 V (*64*), i.e., a spectral typing uncertainty of 0.5 subtypes (*65*). The photosphere parameters (T_{eff}, log *g*, and (Fe/H)) of Gliese 486 were

adopted from previous compilations by (*66*) that used CARMENES spectra. The bolometric luminosity was taken from (*12*) and the T_{eff} from (*66*); combining these with the Stefan-Boltzmann law, we calculated the stellar radius. The mass-radius relation of (*13*), was used to determine the stellar mass.

Gliese 486 is an M dwarf with very weak chromospheric activity (*67,68,69*). It is a slow rotator with very narrow spectroscopic lines (*70, 71*), faint Ca II H&K emission (*72, 73*), and weak magnetic field (*74*). A log R'_{HK} was calculated by averaging the HIRES S_{MWO} index series after discarding three obvious outliers and a fourth datum with a low S/N. The mean S_{MWO} corresponds to log $R'_{\text{HK}} = -5.51\pm0.39$ and an expected rotation period of ~90 d (using the relations of (*70*) and the V and Ks magnitudes of (*75*) and (*76*), respectively). The mean value of log R'_{HK} from the HIRES data is higher than that from HARPS data (*70*), but consistent within 1σ, and the larger uncertainty arises from intrinsic variability of the Ca II H&K doublet.

We used the photometric data sets of SuperWASP and ASAS-SN to measure the stellar rotation period of Gliese 486. After accounting for the discrete Fourier transform window functions of the observations, three significant peaks appear in the periodograms (Fig. S3), at approximately 189 d, 125 d, and 93 d, similar to the 1/2, 1/3, and 1/4 yearly harmonics at 182.62 d, 121.75 d, and 91.31 d that could be produced by the observing schedule. These were visible only in the SuperWASP-North dataset (with the longest time baseline and smallest wrms) and for Gliese 486, as no other SuperWASP comparison star of similar brightness in the same field of view displayed those peaks. A corresponding peak at about 125-130 d appears with false alarm probability (FAP) ≈ 1 % in the Lomb-Scargle periodograms (GLS) (*77*) of ASAS-SN g' and CARMENES VIS Hα data (see below). This is consistent with the periods estimated from log R'_{HK}, suggesting the SuperWASP-North peak at ~ 125 d is real. We modelled the SuperWASP and ASAS-SN data using a quasi-periodic Gaussian process (GP) analysis, following (*78*) using the JULIET library (*53*) library. We used the exp-sin-squared kernel multiplied with a squared-exponential kernel and produced nightly bins for the photometric data. We fitted an offset and a jitter term (in quadrature to the diagonal of the resulting covariance matrix of the GP) and applied distinct GP hyperparameters for the amplitudes for each instrument and photometric band. Global GP hyper-parameters we used for the time scale of the amplitude modulation and the rotation period. This analysis indicated a stellar rotation period $P_{\text{rot,GP}} = 130.1^{+1.6}_{-1.2}$ d.

Joint transit and RV analysis

Tools

For data and orbital analysis of the Gliese 486 system, we employed the EXO-STRIKER exoplanet toolbox (*21, 79*) to produce a generalized Lomb-Scargle periodogram (GLS) (*77*), a maximum likelihood periodogram (MLP) (*80, 81*), transit photometry detrending using the *wōtan* code (*82*), and transit period search using the transit least squares (TLS) package (*83*). For orbital parameter analysis, the EXO-STRIKER offers a fast RV and transit best-fit optimization and sampling schemes such as Markov chain Monte Carlo (MCMC) sampling using the EMCEE sampler (84) and the nested sampling technique (85) with the DYNESTY sampler (*86*), which were coupled with the CELERITE package (*87*) for GP regression analysis. To build transit light curve

models, and extract transit timing variations (TTV), the Exo-Striker uses the BAsic Transit Model cAlculatioN package (batman) (*88*).

We also used the juliet library (*53*) for GP analysis of the ground-based photometry data and for comparison with the Exo-Striker analysis.

Periodogram analysis

We computed the MLP for period search in RVs and activity indices of Gliese 486. The MLP implementation is similar to a GLS periodogram, but allows for multiple data sets, each with an additive offset and a jitter term (*80*). The log likelihood (ln L) is optimized for each test frequency. Because the MLP fits more parameters, MLP is more computationally expensive than the GLS periodogram, but the MLP is more appropriate for a period search in combined RV data sets that have an unknown variance (that is, RV jitter). We adopted significance thresholds of the likelihood improvements with respect to a model constructed from the same parameters but with zero amplitude, that correspond to false-alarm probabilities of 10%, 1%, and 0.1%. Fig. S4A shows the MLP periodograms of the CARMENES VIS and NIR, MAROON-X red and blue, HIRES, and HARPS RV time series, separately and combined. The CARMENES VIS and the MAROON-X red and blue data each indicate significant power (FAP < 0.1%) at a period of 1.467 d, much shorter than the stellar rotation period. The MAROON-X data have a short temporal baseline of only ~13.2 d, so the Δln L power spectrum has lower resolution than the CARMENES, HARPS, and HIRES data, Nevertheless, the MAROON-X data has significant (FAP < 0.1%) power at frequency consistent with the same period. Another strong peak in the CARMENES VIS and MAROON-X periodograms appears at the 1 d alias frequency f_{alias} of the planetary period in the form of $f_{alias} = f_{1d} - f_{planet\ period} \approx 0.31834$ d^{-1} (leading to an alias period of $P_{alias} \approx 3.14$ d), which is no longer seen when the signal of Gliese 486 b is subtracted.

For stars of spectral types M3-4 V, such as Gliese 486, the spectroscopic information (i.e., the number of deep spectral lines) needed for precise RV measurements is not very abundant in the CARMENES NIR spectra (*10, 37*). We find that the 60 CARMENES NIR RVs are less precise and do not have any significant peak with FAP < 0.1% in the MLP periodogram. The HIRES and HARPS data separately do not show significant power with FAP < 0.1% at any frequency either, but the HARPS data set consists of only 12 measurements, while the HIRES dataset consists of 26 measurements with lower precision. The MLP periodogram of the combined data set shows power at 1.467 d, which is dominated by the CARMENES VIS and MAROON-X RVs. The combined data residuals of the joint transit-RV one-planet model (see **below)** do not show other significant periods.

The MLPs of the CARMENES activity indicators are shown in Fig. S4B. Except for the Hα index, none of them displays signals with significant power of FAP < 0.1% at periods between 1 d and 500 d, in line with previous studies indicating Gliese 486 is a low activity star. The Hα MLP has a strong peak at 1/354 d^{-1} and another weaker one, but marginally significant (FAP ~ 1 %), at 1/130 d^{-1}. The MLP periodograms of the MAROON-X activity indicators are shown in Fig. S4C. Activity indicators of MAROON-X such as the CRX, Na I D, and Ca IRT do not indicate any significant level of activity in the red and the blue channel. The differential line width and Hα show some marginally significant periodicity (FAP ~ 1 %) in both channels,

but without a clear sign of correlation with the RVs over the short MAROON-X temporal baseline.

Joint modeling fitting

For the joint fit analysis, we used only data that showed significant RV signal with FAP < 0.1%, or transit light curves, consistent with the presence transit events of Gliese 486 b. The used RV datasets were CARMENES VIS and MAROON-X blue and red, whereas we did not use HIRES and CARMENES NIR due their intrinsic large RV scatter and insufficient precision. We found that the HARPS SERVAL RVs generally agree in phase and amplitude with Gliese 486 b, but their overall statistical weight was much smaller than those of CARMENES and MAROON-X, and thus we decided not to include these data in the orbital analysis either. The transit photometry data that we used for the analysis were: TESS Sector 23, the two transit events recorded with MuSCAT2 on 9 May 2020 and 12 May 2020 (hereafter $MuSCAT2_1$ and $MuSCAT2_2$), and the three transit events recorded with LCOGT on 15 May 2020, 24 May 2020, and 5 June 2020 (hereafter $LCOGT_1$, $LCOGT_2$, and $LCOGT_3$). The TJO data and the remaining MuSCAT2 transit data have insufficient precision for precise transit analysis. For increasing the transit signal in the MuSCAT2 data, we combined the four light curves into a single one including *g*, *r*, *i*, and *zs* photometry. All RV and transit data time series are taken in the common time frame of Barycentric Dynamical Time (TDB).

In the first step of our modeling we inspected the PDC TESS light curves. Although the PDC dataset was already corrected for dominant systematics by default, we further corrected it for small systematics, which were still evident in the light curve. In particular, we rejected a dozen obvious outliers and normalized the PDC light curve by fitting a Stochastically-driven, damped Harmonic Oscillator (SHO) GP kernel (included in the EXO-STRIKER via CELERITE, 89*)* to capture the non-periodic variation of the light curve. The final product of our detrending was a nearly flat, normalized, TESS light curve, which we adopted to seek for transit signals using TLS. As illustrated in Fig. S5A, we detected a significant TLS signal with false positive rate of < 1% (85), with a period of 1.467 d (as in CARMENES VIS and MAROON-X RV data), together with its harmonics at 0.73 d, 2.93 d, 4.40 d, etc. in Fig. S5B shows the TLS power spectrum of the TESS light curve of the joint fit residuals, which have no evidence of additional transit events.

As a second step, using the TESS PDC photometry, we constructed a transit light curve model with planetary orbital parameters: period P_b, eccentricity e_b, argument of periastron ω_b, inclination i_b, time of inferior transit conjunction t_0, and the planet semi-major axis and radius a_b and R_b (in units of stellar radius, $R_\star$), respectively. The TESS data parameters adopted in our model were the flux offset and jitter parameters, $TESS_{off}$ and $TESS_{jitt}$. The TESS light curve was detrended simultaneously by the SHO GP model with three hyper-parameters: power S_0, characteristic frequency ω_0, and a quality factor of the SHO kernel. We adopted a quadratic limb-darkening model to describe the transit signal shape, adding two more parameters, u_1 and u_2. We then included the RV model, which added seven additional parameters applied to the RVs. For the CARMENES VIS and MAROON-X red and blue datasets we fitted for the RV offsets, RV jitters, and the RV signal semi-amplitude *K*, which constrains the planetary mass.

The rest of orbital parameters are common for the transit and RV model components. In total, the joint model has 21 data and orbital free parameters.

As an alternative analysis, we built a more complex joint model including the MuSCAT2 and LCOGT photometry. For modeling the TESS, MuSCAT2, and LCOGT light curves together with the RVs from CARMENES VIS and MAROON-X red and blue, we adopted different quadratic limb-darkening models and optimized the quadratic limb-darkening parameters for each instrument with six parameters: TESS u_1 and u_2, MuSCAT2$_{1,2}$ u_1 and u_2, and LCOGT$_{1,2,3}$ u_1 and u_2. The ground-based transit MuSCAT2 and LCOGT data were simultaneously detrended with a linear model against airmass at the time of measurement, thus adding five more parameters. We also varied the flux offset and jitter parameter of each transit light curve data separately, which translated into six offset and six jitter transit data parameters. In total, this alternative model has 40 free parameters.

For the modelling fitting process, we adopted a dynamical nested sampling with DYNESTY, with 100% weight on the posterior convergence (86). For all parameters we adopted priors, which are summarized in Table S5. Our nested sampling test represented a forced, high-density, multi-dimensional parameter volume search, the posterior estimates of which were adopted as our final results. The parameter posterior estimates of the two joint models described above (hereafter CMT - for the model including CARMENES VIS, MAROON-X and TESS, and CMT+LM, for the model that adds *LCOGT*, and MuSCAT2) are summarized in Table S6. Fig. 1 shows the phase-folded CMT data and model, Fig. S6 shows the TESS*,* MuSCAT2$_{1,2}$, and LCOGT$_{1,2,3}$ flux time series and the transit light curve component of the CMT+LM model, and Fig. S7 shows the detrended phase-folded data of the CMT+LM model. The posterior distributions of the nested sampling parameters of both models are shown in the corner plots of Figs. S8 and S9, respectively. Both models are consistent with each other within the estimated uncertainties, although the CMT+LM model has larger parameter uncertainties. We attribute this to the much larger parameter space (21 versus 40 parameters), which produces additional covariance with the orbiting parameters. The noisier MuSCAT2 and LCOGT data with respect to TESS do not contribute substantial information to the orbital and physical determination of Gliese 486 b. Therefore, in Table 1 and the reminder of our analysis we report only the parameters obtained from the CMT model.

The orbital eccentricity of Gliese 486 b is not constrained. Our full-Keplerian modelling was done with free e_b, ω_b, or $e_b\sin(\omega_b)$, $e_b\cos(\omega_b)$ parameterization, and both solutions provided only an upper limit on the eccentricity of $e_b < 0.05$ at the 68.3% confidence level. A forced circular model of Gliese 486 b with e_b fixed at 0 (but t_0 varied to assure transit event at $t_0 \sim$ 2458931.16) led to solutions which are statistically indistinguishable from the full Keplerian model. The CMT model has a Bayesian log-evidence of ln $Z = 76406.2 \pm 0.4$ for the circular model and ln $Z = 76405.1 \pm 0.4$ for the full-Keplerian model. The CMT+LM model is similar: ln $Z = 84642.6 \pm 0.4$ for the circular model and ln $Z = 84641.7 \pm 0.4$ for the full-Keplerian model. This low orbital eccentricity is what we expect given the planet's proximity to the star, which should cause tidal circularization. We investigated the star-planet tides of the Gliese 486 system using the EQTIDE code (*22*), which calculates the tidal evolution of two bodies based on standard models (*89, 90, 91*). For Gliese 486 b we adopted the Earth's value $k_2/Q = 0.025$ from (*92*) and

initial planetary rotational period of 0.5 d, whereas for the star Gliese 486 we adopted $k_2/Q = 2 \times 10^6$ and an initial stellar rotational period of 130 d. Fig. S10 shows the eccentricity decay due to star-planet tides from our tidal evolution simulations. We tried a set of different initial semi-major axes and eccentricities a few percent larger than the observed, and found that Gliese 486 b reached synchronous rotation within < 10 000 yr and that, on average, its planetary orbit was fully circularized in only ~ one million years. For our final orbital solution of Gliese 486 b, we therefore adopted the simpler circular orbit model. Our final orbital solution for Gliese 486 b is given in Table 1.

The CARMENES VIS data show small residual scatter of wrms = 1.87 m s^{-1} and an RV jitter level of 1.45 m s^{-1}. MAROON-X blue channel data show wrms = 1.12 m s^{-1} and an RV jitter level of 0.70 ms^{-1}, while the red channel shows wrms = 0.42 m s^{-1} and an RV jitter level of only 0.25 m s^{-1}. The MAROON-X red radial velocities have the lowest scatter ever seen for an M dwarf without applying corrections for activity-induced jitter.

Search for transit timing variations

To search for possible TTVs , we performed two independent analyses including all detected transit data available. The first was done using the EXO-STRIKER by adopting the CMT-LM model, but allowing for variable transit mid times. In this model, the orbital period P_b was fixed at its best-fitting value, while the transit times t_0 to t_{52} were allowed to vary (but only fitting the 18 individual times-of-transits for which we had data), thus adding 16 more fitting parameters to the base model. The second test was done with JULIET, which was applied only to the transit data. In this scheme, all the transit parameters across each individual TESS, MuSCAT2, and LCOGT transit were shared, except for the limb-darkening coefficients (which were individual to each instrument), the 18 individual times-of-transits, out-of-transit fluxes, and the coefficients of linear models in airmass, which were used to detrend each of the ground-based light curves simultaneously in the modelling procedure.

We detected some marginal TTVs in the order of a few minutes in the *TESS* data, and larger variations on the LCOGT transits, but with higher TTV uncertainty. Using the EXO-STRIKER and JULIET we qualitatively compared a fit using a linear ephemeris (that is, non-TTV model) and a model that allows TTVs. We found a very strong Bayesian evidence in favor of a linear ephemeris i.e., no significant TTVs arising from the combined transit photometry ($\Delta \ln Z \sim 44$ in the case the EXO-STRIKER, $\Delta \ln Z \sim 37$ in the case of JULIET). We also used the EXO-STRIKER to dynamically model the extracted TTVs, but we could not explain these variations by another non-transiting planet perturbing Gliese 486 b. This is consistent with the RV data, which did not show any evidence for another planet. We conclude that there is no reason to prefer TTVs over linear ephemeris and evidence of only a single planet Gliese 486 b.

Supplementary Text

Prospects for atmospheric investigation of Gliese 486 b

Fig. 3A shows the expected transmission signal of the planetary atmospheres of all known rocky

planets (with R_p between 0.5 and 2.0 R_E) with measured masses and radii that transit M dwarfs as a function of the host star magnitude in the Ks band. In all cases, a mean molecular weight $\mu = 18$ for a water (steam)-dominated atmosphere was assumed. Higher transmission signal values around bright stellar host magnitudes provide more favorable conditions for detecting a possible atmosphere, while planets with lower transmission signals around faint stars are more technically challenging to characterize. Three target sub-groups are apparent. The first is rocky planets transiting around very bright host stars, visible with the naked eye from dark sites. These are generally G- and K-type main-sequence stars, and the prospects for their atmospheric investigation and characterization are higher because of the host star brightness. Members of this group are 55 Cnc e (*30*), HD 219134 b and c (*93*), and BD-02 5958 b and c (*94*) (π Men c (*95*), with a density of about $2.8 \cdot 10^3$ kg m^{-3}, is not a rocky planet). However, except for the poorly understood variability of 55 Cnc e (*96*), none has a detected atmosphere. The second group are planets orbiting M-dwarf hosts have better prospects for atmospheric detection, as the small size of the host star compensates for their much dimmer brightness. In this group, the largest atmospheric signals are expected for the TRAPPIST-1 planets because of the high radius ratio between the planets and the host star. Gliese 486 b is also favorable for rocky planet atmosphere searches. Gliese 486 b is similar to GJ 357 b (*97*) in terms of planet parameters and prospects for atmospheric investigation. These planets have similar suitability: the known super-Earths around non-M stars, Gliese 486 b, and the TRAPPIST-1 system. A continuously updated compendium of transiting planets with measured mass around M dwarfs is available in (*98*).

The combination of its small radius and high equilibrium temperature makes Gliese 486 b unlikely to have retained a large atmosphere. With a radius of about 1.3 R_E, we expect Gliese 486 b to have lost its primordial hydrogen-helium atmospheres due to photoevaporation processes (*29, 99, 100*). At the current planet location the atmosphere could have been lost during the earlier phases of Gliese 486 stellar evolution. However, whether rocky planets around M dwarfs are able to retain a substantial fraction of their atmospheres and, if so, at which ranges of mass and T_{eq} remains an open question. Gliese 486 b could be used to test these mechanisms.

At present, LHS 3844 b, a 1.3 R_E planet around an M5 V star, is the most thoroughly investigated small rocky planet in search for an atmosphere. Its thermal phase curve has been searched for signs of atmospheric heat redistribution (101). Those authors determined that the data were best explained by a bare rock model with a low Bond albedo, supporting theoretical predictions that hot terrestrial planets orbiting small stars may not retain substantial atmospheres (*99, 102*). However, LHS 3844 b has an orbital period 3.2 times shorter than Gliese 486 b and T_{eq} hotter by 100 K. LHS 3844 b does not have a measured mass limiting interpretation of its atmosphere. The brightness of the host star makes Gliese 486 b a more suitable target for phase curve characterization and epoch of superior transit conjunction (secondary eclipse time) determination and, thus, determining the day and night side temperatures of the planet. Our joint model with free planet eccentricity constrains the secondary eclipse time to $2458931.88643\,^{+0.00769}_{-0.00829}$ d, suitable for scheduling future observations.

Table S1. Radial velocity time-series from the CARMENES VIS channel spectra. Only a subset of the data analysed in this paper is shown here. A machine-readable version of the full dataset, including the spectroscopic activity indices is available in Data S1.

Barycentric Julian Date, BJD	Radial velocity, RV (m s^{-1})	Radial velocity uncertainty, σRV (m s^{-1})
2457400.74081	4.52	1.07
2457401.74239	0.07	1.30
2457418.71847	-2.32	1.14
2457421.70507	-2.65	0.98
2457426.69298	0.91	1.10
2457442.60293	-2.97	0.91
2457442.62657	-3.46	0.93
2457476.51979	-2.88	1.35
2457492.53441	-1.28	1.62

Table S2. Radial velocity time-series from the CARMENES NIR channel spectra. Only a subset of the data analysed in this paper is shown here. A machine-readable version of the full dataset, including the spectroscopic activity indices is available in Data S1.

Barycentric Julian Date, BJD	Radial velocity, RV (m s⁻¹)	Radial velocity uncertainty, σRV (m s⁻¹)
2457788.52216	-24.63	10.92
2457802.65175	-4.70	5.12
2457856.53224	-19.15	4.22
2457876.53529	-16.20	4.48
2457896.4259	-15.63	3.89
2457950.37141	-17.72	9.92
2458122.69387	-12.63	3.94
2458141.58966	-14.78	4.94
2458206.57208	-11.17	5.61

Table S3. Radial velocity time-series from the MAROON-X red channel spectra. Only a subset of the data analysed in this paper is shown here. A machine-readable version of the full dataset, including the spectroscopic activity indices is available in Data S1.

Barycentric Julian Date, BJD	Radial velocity, RV (m s^{-1})	Radial velocity uncertainty, σRV (m s^{-1})
2458989.74702	1.74	0.46
2458989.75182	1.37	0.40
2458991.82562	-2.38	0.40
2458991.83039	-1.98	0.34
2458992.85416	-0.58	0.27
2458992.85888	-1.02	0.40
2458993.82807	4.14	0.30
2458993.83285	4.17	0.46
2458994.77985	-2.26	0.72

Table S4. Radial velocity time-series from the MAROON-X blue channel spectra. Only a subset of the data analysed in this paper is shown here. A machine-readable version of the full dataset, including the spectroscopic activity indices is available in Data S1.

Barycentric Julian Date, BJD	Radial velocity, RV (m s^{-1})	Radial velocity uncertainty, σRV (m s^{-1})
2458989.74701	3.30	1.01
2458989.75179	1.72	0.86
2458991.82561	-2.75	0.77
2458991.83037	-3.37	0.84
2458992.85415	-1.55	0.87
2458992.85885	-2.59	0.82
2458993.82806	4.19	1.13
2458993.83284	2.99	1.01
2458994.77982	-2.56	1.68

Table S5. Adopted parameter priors. These prior probabilities were used as input to the modeling of photometry (TESS, MuSCAT2, LCOGT) and radial velocities (CARMENES VIS, MAROON-X red, MAROON-X blue). The notations of *N*, *U*, and *J* represent normal, uniform, and Jeffrey's prior probability distributions.

Parameter	Adopted priors
K_b (m s^{-1})	$U(0.01,5.00)$
P_b (d)	$U(1.46500,1.47500)$
e_b	$U(0.0,0.3)$, or fixed at 0
ω_b (deg)	$U(0.0,360.0)$, or undefined when $e_b= 0$
$e_b\sin(\omega_b)$	$U(-1.0,1.0)$
$e_b\cos(\omega_b)$	$U(-1.0,1.0)$
i_b (deg)	$U(85.00,95.00)$
$t_0 - 2450000$ (BJD)	$U(8931.04,8931.26)$
$a_b/R_\star$	$U(5.00,15.00)$
$R_b/R_\star$	$U(0.01,0.05)$
RV offset CARMENES (m s^{-1})	$U(-5.00,5.00)$
RV jitter CARMENES (m s^{-1})	$J(0.01,5.00)$
RV offset MAROON-X red (m s^{-1})	$U(-5.00,5.00)$
RV jitter MAROON-X red (m s^{-1})	$J(0.01,5.00)$
RV offset MAROON-X blue (m s^{-1})	$U(-5.00,5.00)$
RV jitter MAROON-X blue (m s^{-1})	$J(0.01,5.00)$
Transit offset TESS (ppm)	$N(0.0,1000.0)$
Transit jitter TESS (ppm)	$J(1.0,3000)$

Transit offset MuSCAT2 1,2 (ppm)	$N(0.0, 1000.0)$
Transit jitter MuSCAT2 1,2 (ppm)	$J(1.0, 3000)$
Transit offset LCOGT 1,2,3 (ppm)	$N(0.0, 1000.0)$
Transit jitter LCOGT 1,2,3 (ppm)	$J(1.0, 3000)$
TESS GP SHO S_0	$J(0.0001, 0.0100)$
TESS GP SHO Q	$J(0.0001, 0.5000)$
TESS GP SHO ω_0	$J(0.0001, 2.0000)$
Linear detrend. coef. MuSCAT2$_{1,2}$ & LCOGT$_{1,2,3}$	$U(-0.1, 0.1)$
Quad. limb-dark. TESS u_1	$U(0.00, 1.00)$
Quad. limb-dark. TESS u_2	$U(0.00, 1.00)$
Quad. limb-dark. MuSCAT2 u_1	$U(0.00, 1.00)$
Quad. limb-dark. MuSCAT2 u_2	$U(0.00, 1.00)$
Quad. limb-dark. LCOGT u_1	$U(0.00, 1.00)$
Quad. limb-dark. LCOGT u_2	$U(0.00, 1.00)$

Table S6. Results of the joint fit model fitting. Best fitting values and uncertainties are listed as extracted from the posterior probability distributions of the CMT and CMT+ML models (Figures S8 & S9, respectively).

Parameter	CMT+ML fit	CMT fit
K_p [m s^{-1}]	$3.358\,^{+0.099}_{-0.164}$	$3.371^{+0.070}_{-0.081}$
P_p [d]	$1.467111\,^{+0.000050}_{-0.000026}$	$1.467119\,^{+0.000031}_{-0.000030}$
i_p [deg]	$88.6\,^{+1.0}_{-1.4}$	$88.4\,^{+1.1}_{-1.4}$
t_0 [d]	$2458931.15939\,^{+0.00056}_{-0.00067}$	$2458931.15935\,^{+0.00042}_{-0.00042}$
$a_p/R_\star$	$10.94\,^{+0.55}_{-1.22}$	$10.80\,^{+0.57}_{-1.02}$
$R_p/R_\star$	$0.0366\,^{+0.0011}_{-0.0026}$	$0.0365\,^{+0.0011}_{-0.0014}$
RV off. CARMENES−VIS [m s^{-1}]	$-0.15\,^{+0.31}_{-0.32}$	$-0.19\,^{+0.22}_{-0.23}$
RV off. MAROON−X red [m s^{-1}]	$0.105\,^{+0.084}_{-0.089}$	$0.111\,^{+0.057}_{-0.055}$
RV off. MAROON−X blue [m s^{-1}]	$0.09\,^{+0.20}_{-0.21}$	$0.10\,^{+0.14}_{-0.13}$
RV jitter CARMENES−VIS [m s^{-1}]	$1.42\,^{+0.26}_{-0.37}$	$1.47\,^{+0.22}_{-0.20}$
RV jitter MAROON−X red [m s^{-1}]	$0.258\,^{+0.163}_{-0.080}$	$0.245\,^{+0.071}_{-0.066}$
RV jitter MAROON−X blue [m s^{-1}]	$0.65\,^{+0.24}_{-0.30}$	$0.67\,^{+0.18}_{-0.19}$
Transit offset *TESS* [ppm]	$0\,^{+1900}_{-1800}$	$60\,^{+850}_{-890}$
Transit offset MuSCAT$_1$ [ppm]	$-200\,^{+2000}_{-2100}$	...
Transit offset MuSCAT$_2$ [ppm]	$1300\,^{+1800}_{-1500}$	...
Transit offset LCOGT$_1$ [ppm]	$-2300\,^{+940}_{-1210}$	...

Transit offset LCOGT$_2$ [ppm]	800^{+1900}_{-1700}	...
Transit offset LCOGT$_3$ [ppm]	-3950^{+770}_{-1120}	...
Transit jitter *TESS* [ppm]	$4.6^{+11.5}_{-2.9}$	$4.0^{+6.4}_{-2.3}$
Transit jitter MuSCAT$_1$ [ppm]	24^{+146}_{-21}	...
Transit jitter MuSCAT$_2$ [ppm]	20^{+107}_{-17}	...
Transit jitter LCOGT$_1$ [ppm]	1790^{+210}_{-1250}	...
Transit jitter LCOGT$_2$ [ppm]	34^{+285}_{-31}	...
Transit jitter LCOGT$_3$ [ppm]	930^{+170}_{-710}	...
TESS GP-SHO S$_0$	$0.00102^{+0.00319}_{-0.00078}$	$0.00074^{+0.00320}_{-0.00055}$
TESS GP-SHO Q	$0.0108^{+0.0197}_{-0.0077}$	$0.0093^{+0.0131}_{-0.0063}$
TESS GP-SHO ω_0	$0.27^{+0.46}_{-0.18}$	$0.36^{+0.56}_{-0.20}$
Linear trend MuSCAT$_1$	$0.0014^{+0.0016}_{-0.0015}$	...
Linear trend MuSCAT$_2$	$0.0038^{+0.0014}_{-0.0016}$	...
Linear trend LCOGT$_1$	$-0.00148^{+0.00070}_{-0.00058}$	...
Linear trend LCOGT$_2$	$0.0006^{+0.0012}_{-0.0014}$	...
Linear trend LCOGT$_3$	$-0.00252^{+0.00086}_{-0.00071}$	...
u_1 TESS	$0.29^{+0.25}_{-0.18}$	$0.26^{+0.21}_{-0.16}$
u_2 TESS	$0.39^{+0.30}_{-0.24}$	$0.42^{+0.31}_{-0.26}$
u_1 MuSCAT	$0.48^{+0.25}_{-0.27}$	...
u_2 MuSCAT	$0.52^{+0.29}_{-0.31}$	...
u_1 LCOGT	$0.51^{+0.27}_{-0.28}$	...
u_2 LCOGT	$0.48^{+0.31}_{-0.29}$	...
$M_{\rm p}$ [M$_\oplus$]	$2.80^{+0.14}_{-0.19}$	$2.82^{+0.11}_{-0.12}$

a_{p} [au]	$0.01734\,^{+0.00026}_{-0.00027}$	$0.01734\,^{+0.00026}_{-0.00027}$
R_{p} [$R_{\oplus}$]	$1.305\,^{+0.068}_{-0.107}$	$1.305\,^{+0.063}_{-0.067}$
T_{eq} [K]	$701\,^{+13}_{-13}$	$701\,^{+13}_{-13}$
S [$S_{\oplus}$]	$40.3\,^{+1.5}_{-1.4}$	$40.2\,^{+1.5}_{-1.4}$
g [m s^2]	$16.1\,^{+2.6}_{-1.8}$	$16.2\,^{+1.9}_{-1.6}$
ρ_{b} [10^{-3} kg cm^{-3}]	$6.9\,^{+1.7}_{-1.1}$	$7.0\,^{+1.2}_{-1.0}$
v_{esc} [km s^{-1}]	$16.37\,^{+0.70}_{-0.64}$	$16.44\,^{+0.55}_{-0.52}$
Impact parameter b	$0.27\,^{+0.21}_{-0.18}$	$0.29\,^{+0.20}_{-0.20}$
Transit duration [h]	$1.021\,^{+0.046}_{-0.027}$	$1.025\,^{+0.031}_{-0.023}$
$\rho_{\star}$ [10^{-3} kg cm^{-3}]	$11.5\,^{+1.8}_{-3.4}$	$11.1\,^{+1.9}_{-2.8}$
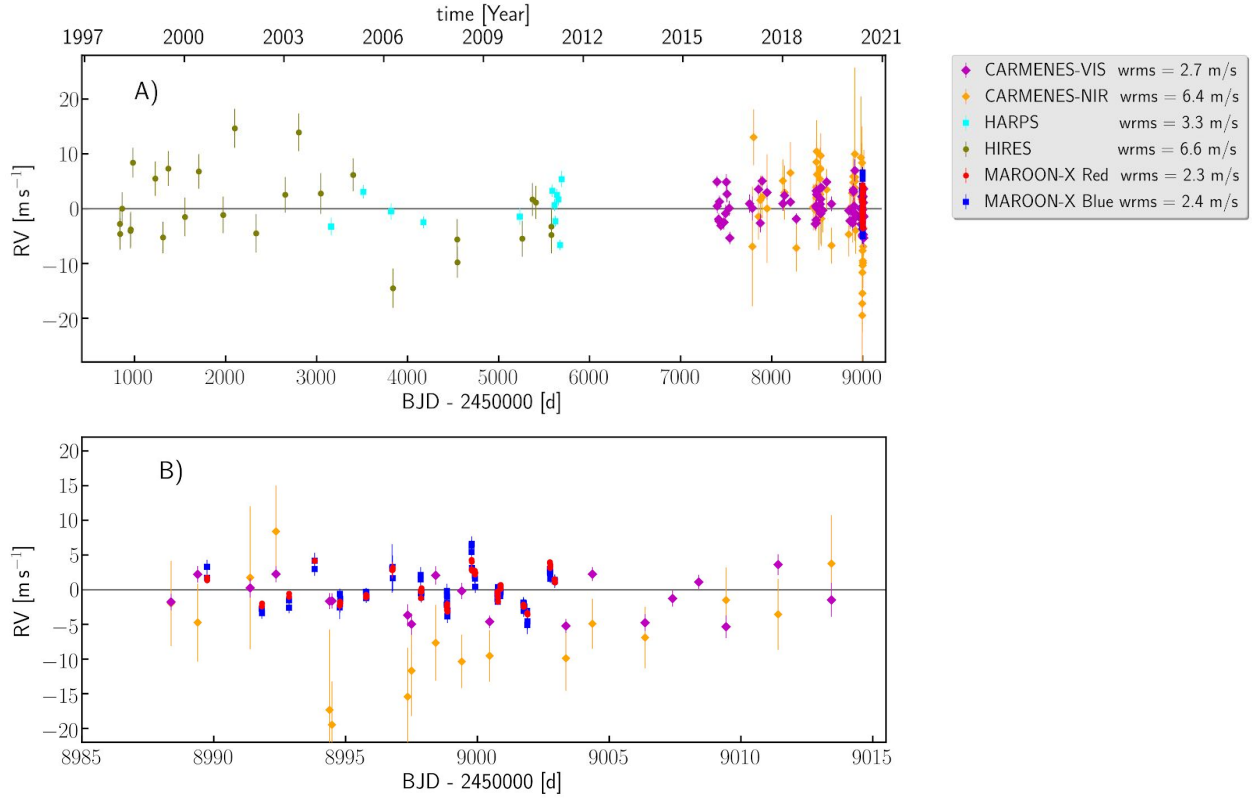
Fig. S1. RV data for Gliese 486. Panel **(A)** shows 27 HIRES RVs (green circles), 12 HARPS RVs (cyan squares), 76 CARMENES VIS RVs (magenta diamonds), 60 CARMENES NIR (amber diamonds), and 65 MAROON-X blue (blue squares) and red (red circles) RVs. The data error bars indicate the 1σ uncertainties of the measurements. The time baseline of the observations is from January 1998 to May 2020. A HIRES outlier at BJD = 2452006.986 (RV ~ −38 m s^{-1}) falls outside of the plotting range. Calendar years are indicated at the top for reference. Panel **(B)** shows a zoomed baseline between BJD = 2458985 and 2459015 when high-cadence RVs were obtained.
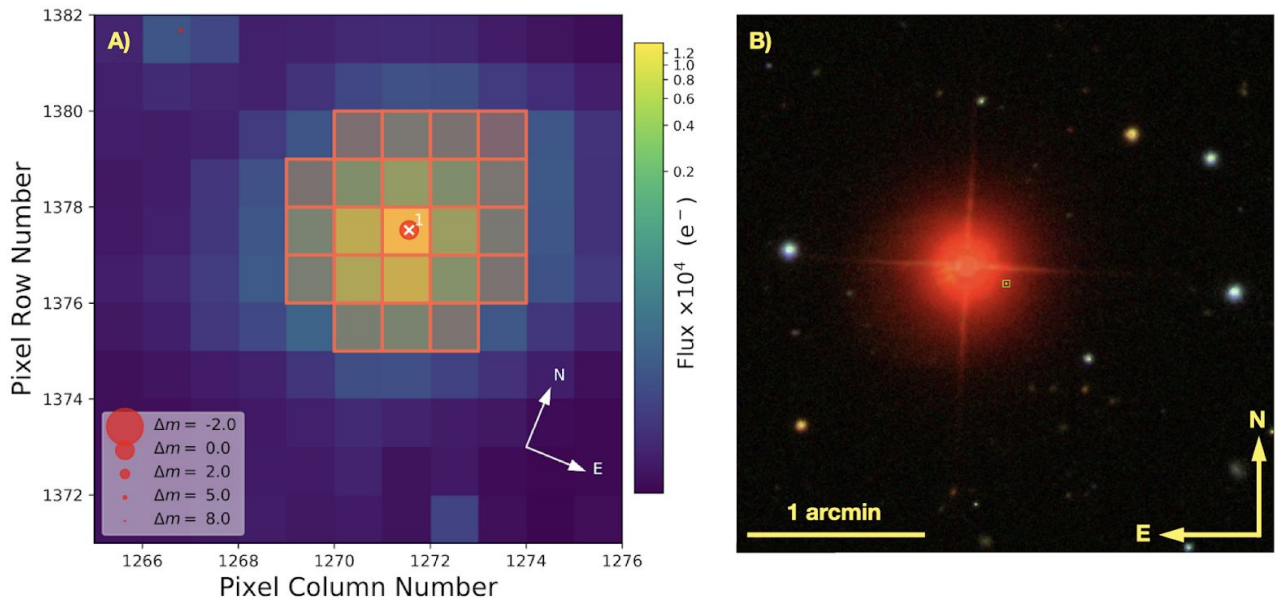
Fig. S2. *TESS* **Sector 23 TPF and a false-color, 3×3 arcmin^2 SDSS9 image of Gliese 486. (A)** The TPF electron counts are color-coded by flux, the orange bordered pixels are used in SAP, and the scale is 21 arcsec pixel^{-1}. **(B)** A green square in the *g'r'i'* SDSS9 (*52*) composition (epoch of observation: J2003.32) marks the location of the star in early 2020. In both fields of view, Gliese 486 is the brightest star.
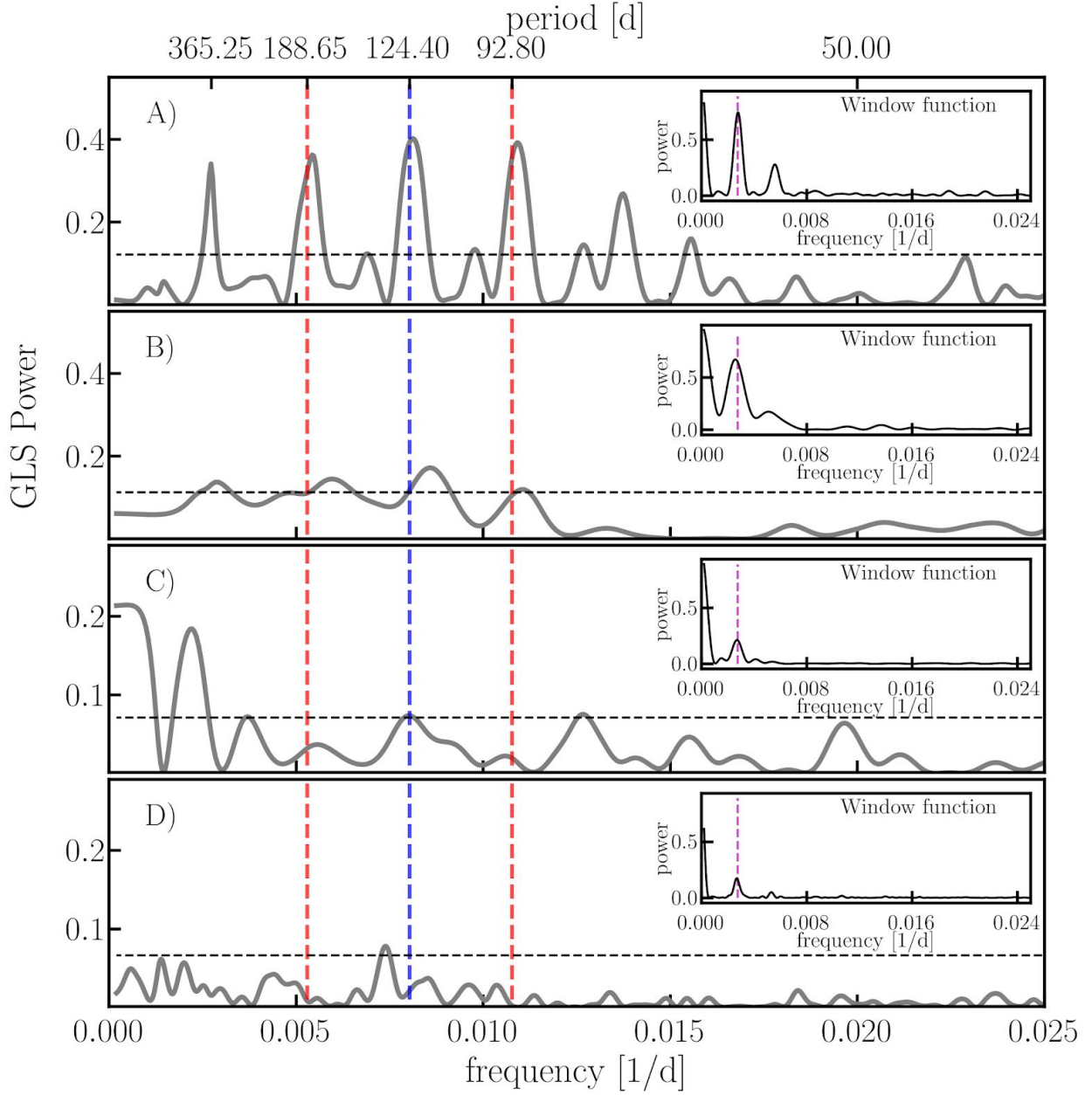
Fig. S3. GLS power spectrum of the photometric data from SuperWASP and ASAS-SN of Gliese 486. (A) SuperWASP North, **(B)** SuperWASP South, **(C)** ASAS-SN *g'* and **(D)** ASAS-SN *V* band ground-based photometry. The inset panels show the discrete Fourier transform window function of the observations. The blue vertical dashed line indicates a peak that is close to the most likely stellar rotational period of Gliese 486 obtained from GP ($P_{rot} \sim 130$ d), while the red vertical dashed lines indicate the first two one-year aliases of this signal.
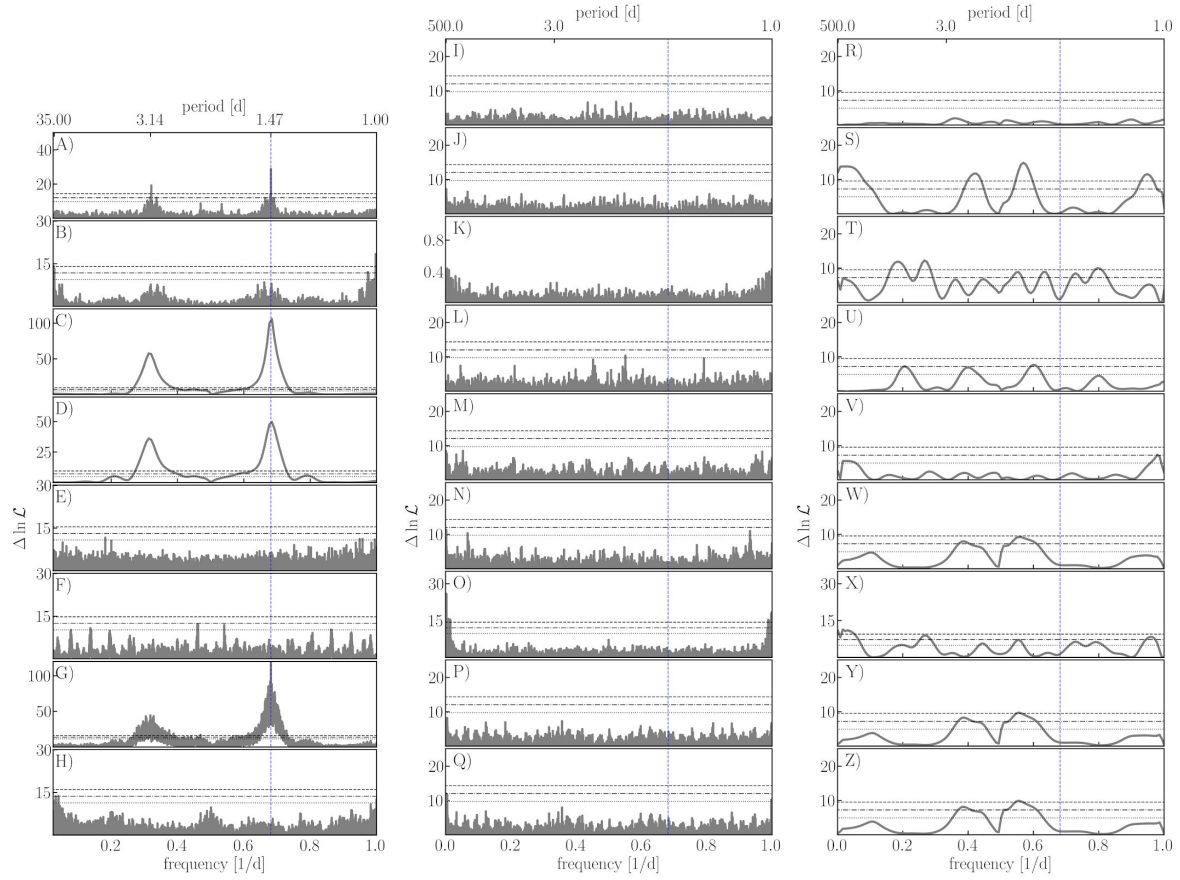
Fig. S4. Maximum logarithmic likelihood periodograms of the spectroscopic data of Gliese 486. Left panels are **(A)** CARMENES VIS RVs, **(B)** CARMENES NIR RVs, **(C)** MAROON-X red RVs, **(D)** MAROON-X blue RVs, **(E)** HIRES RVs, **(F)** HARPS, **(G)** all RVs together, **(H)** best-fit residuals of all RVs; middle panels are **(I)** CARMENES-VIS BIS, **(J)** CARMENES-VIS CON, **(K)** CARMENES-VIS FWHM, **(L)** CARMENES-VIS Ca IRT, **(M)** CARMENES-VIS CRX, **(N)** CARMENES-VIS dLW, **(O)** CARMENES-VIS Hα, **(P)** CARMENES-VIS Na D1, **(Q)** CARMENES-VIS Na D2; right panels are **(R)** MAROON-X red CRX, **(S)** MAROON-X red dLW, **(T)** MAROON-X red Hα, **(U)** MAROON-X red Ca IRT, **(V)** MAROON-X blue CRX, **(W)** MAROON-X blue dLW, **(X)** MAROON-X blue Hα, **(Y)** MAROON-X Na D1, **(Z)** MAROON-X Na D2. Panels **(A)-(H)** show only the period range of 1-40 d (no significant lower frequency signals are detected in the RV data). The orbital frequency of Gliese 486 b is P_b = 1.467 d (blue dashed vertical line) is apparent in the CARMENES VIS and MAROON-X data. The second strongest peak at ~3.14 d is the 1 d alias frequency. Horizontal lines indicate the $\Delta \ln L$ significance levels that correspond to FAP = 10% (dotted), 1% (dot-dashed), and 0.1% (dashed).
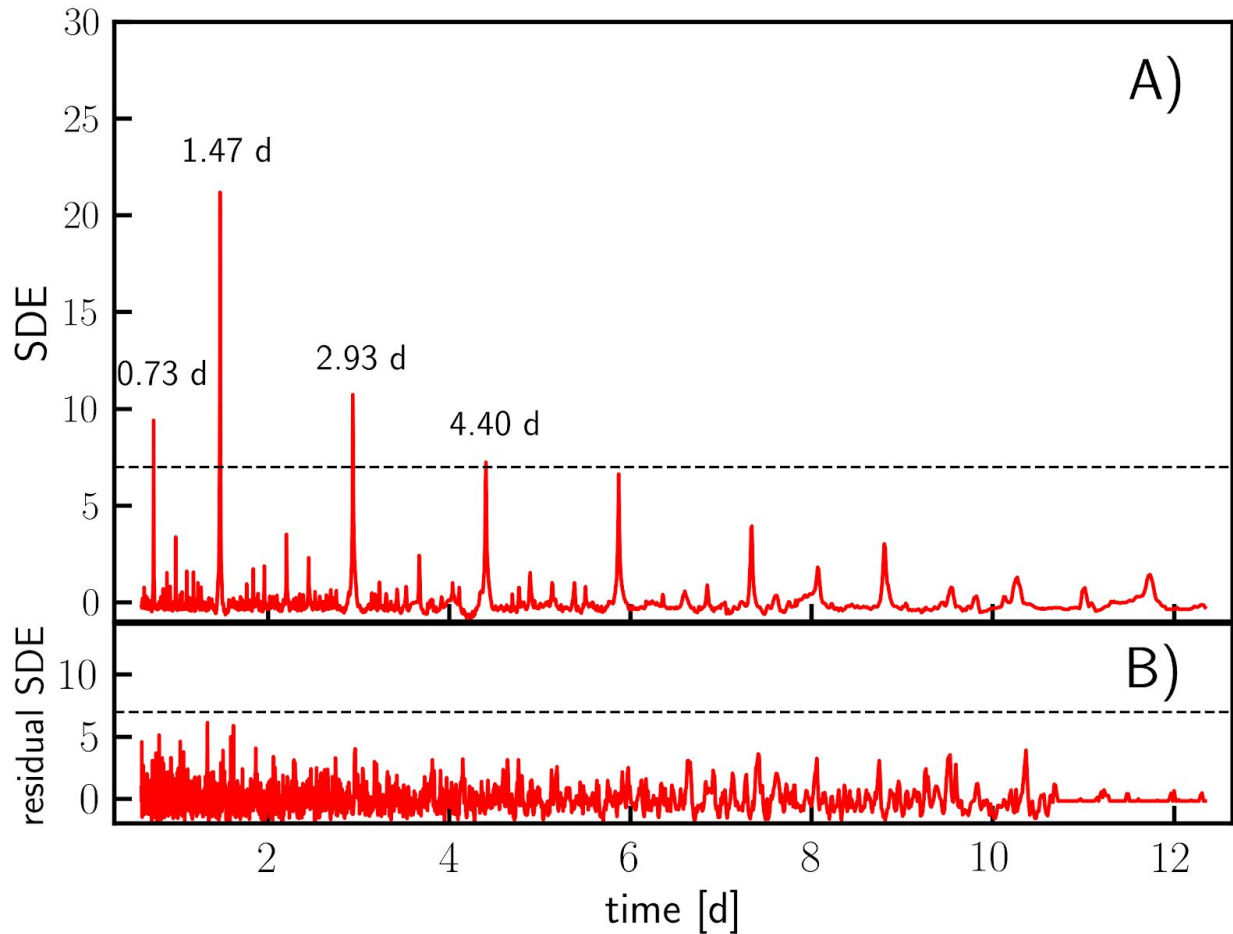
Fig. S5. TLS power spectra of the detrended TESS Sector 23 PDC light curve of Gliese 486.
(A) The planetary transit signal at $P_b = 1.467$ d is accompanied by harmonics at 0.73, 2.93, and 4.40 d. **(B)** TESS residuals of the one-planet transit model. The horizontal dashed line indicates the signal detection efficiency (SDE) power level of 7.0, which corresponds to a TLS false positive rate of 1 % (85).
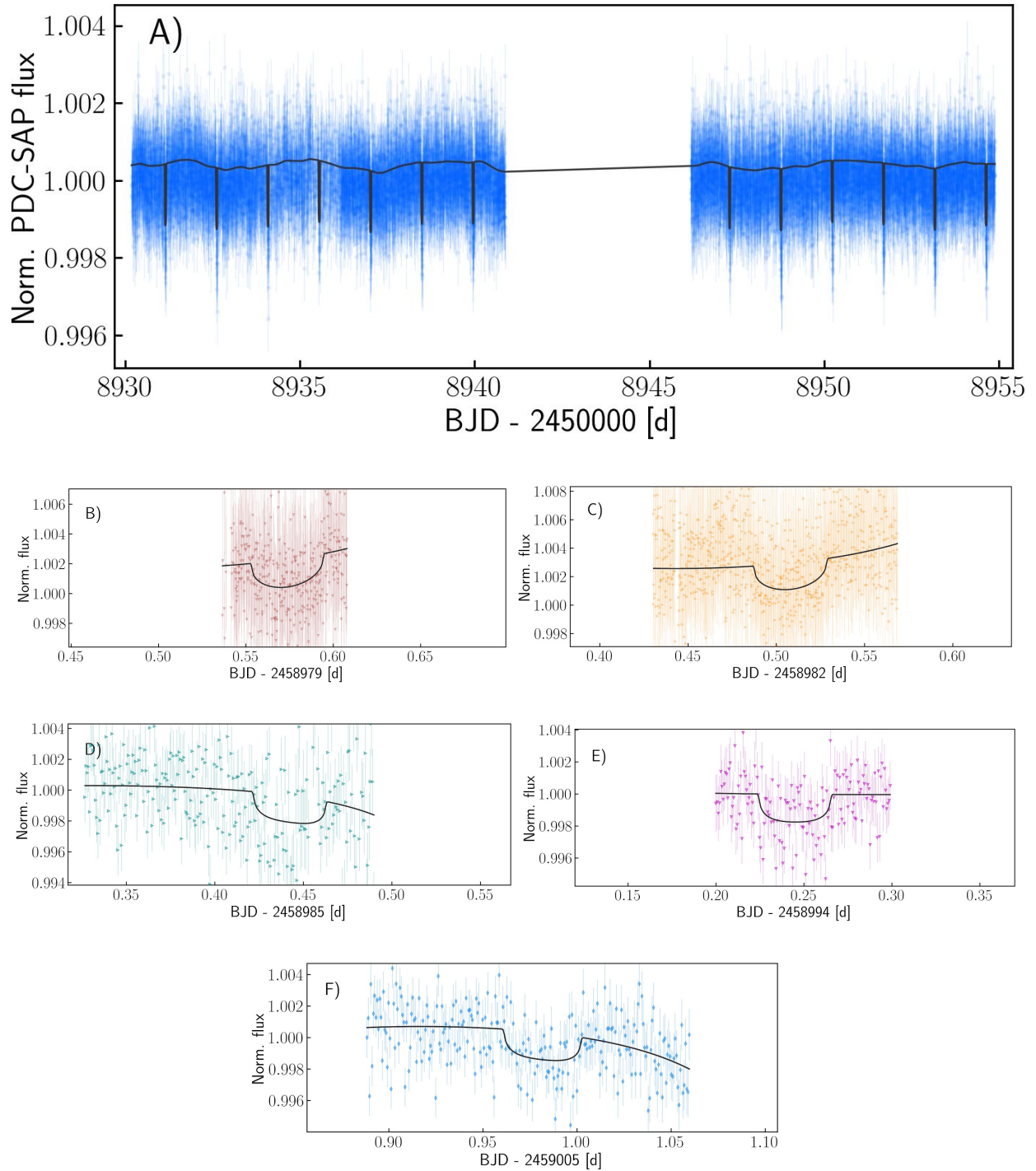
Fig. S6. Transit photometry of Gliese 486. The transit component of the joint model is shown with a black solid line. (A) PDC data from Sector 23 of *TESS*. (B) Ground based data of Gliese 486 from MuSCAT2$_1$ and (C) MuSCAT2$_2$. (D) Ground based data of Gliese 486 from LCOGT$_1$, (E) LCOGT$_2$, and (F) LCOGT$_3$. Error bars indicate 1σ uncertainties of individual measurements.
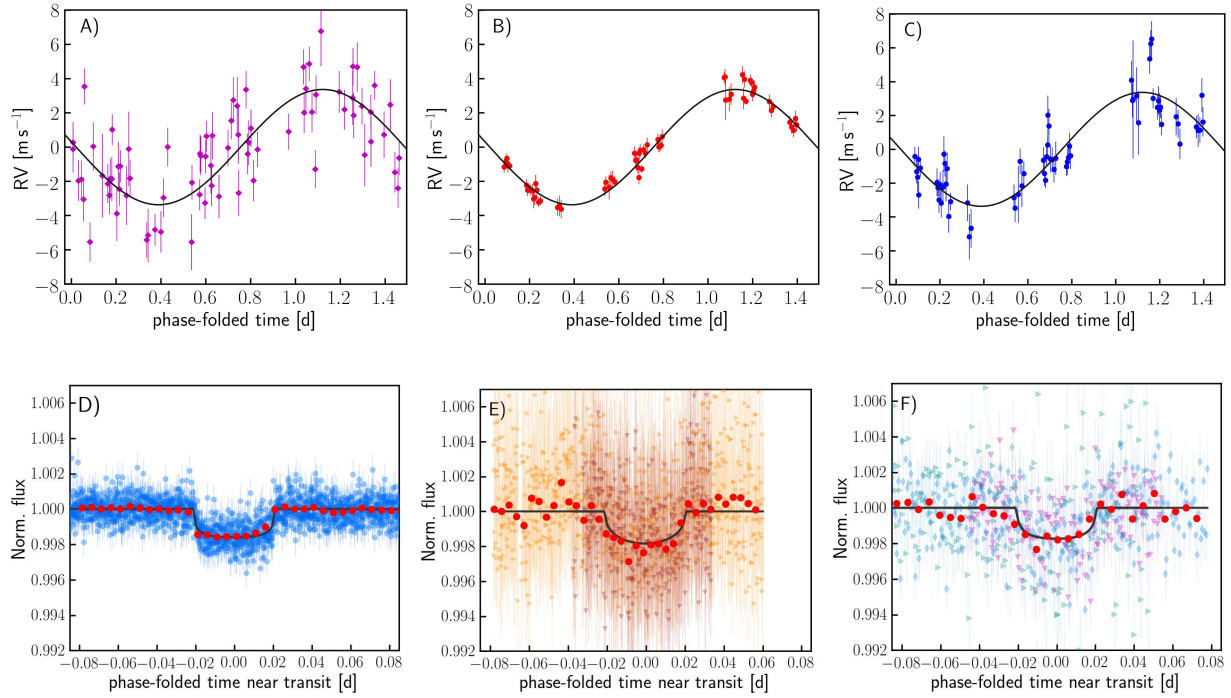
Fig. S7. Same as Fig. 1, but for the CMT+LM model and datasets. Phase-folded CARMENES VIS **(A)**, MAROON-X red **(B)**, and MAROON-X blue RV data **(C)**. Phase-folded sector 23 *TESS* data **(D)**, MuSCAT2 data obtained on two nights (9 May 2020: amber, 12 May 2020: brown) **(E)**, and LCOGT data obtained on three nights (15 May 2020: cyan, 24 May 2020: magenta, 5 June 2020: light blue) **(F)**. Error bars indicate 1σ uncertainties of individual measurements.
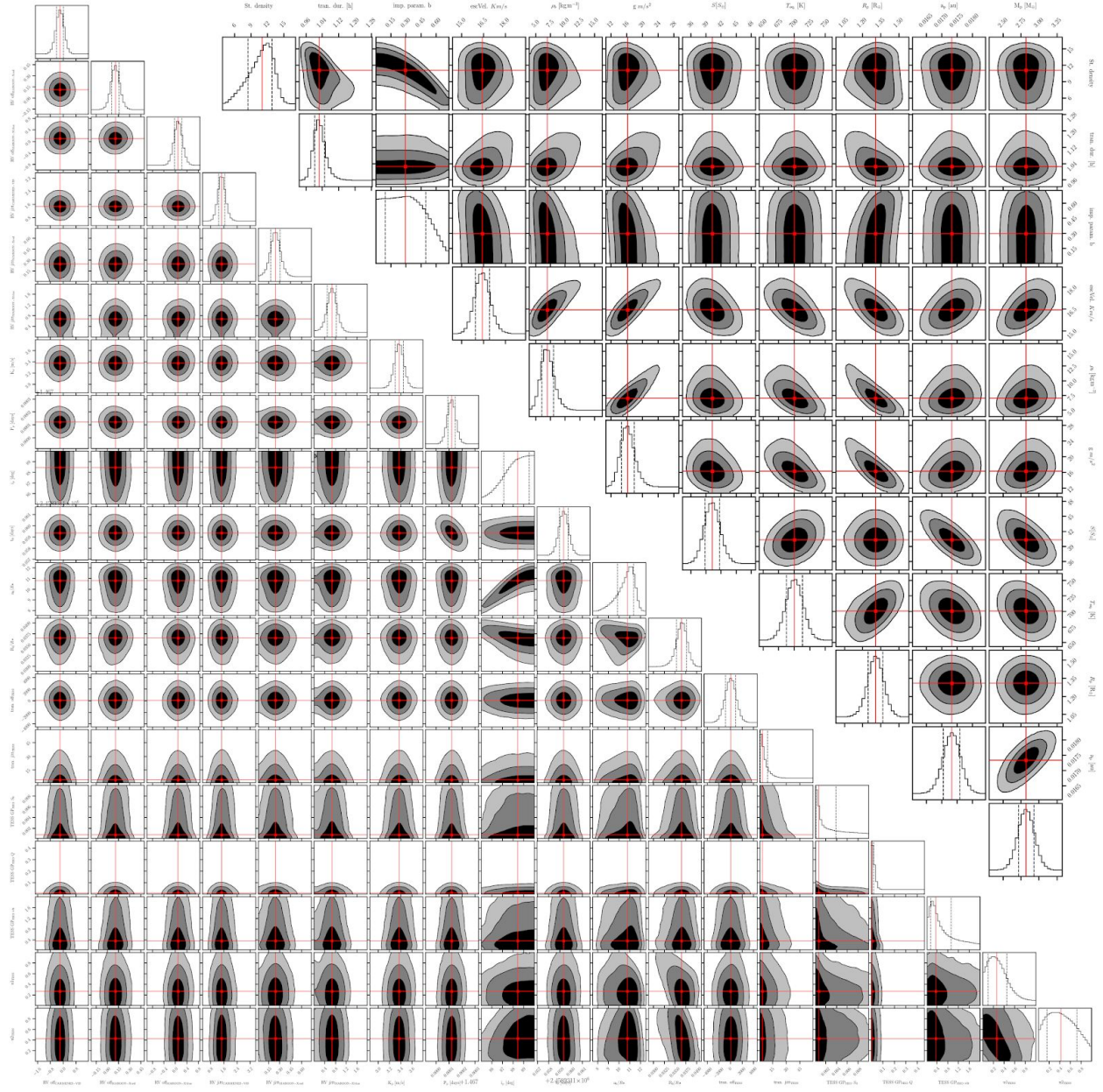
Fig. S8. Results of the CMT model fitting. Lower left correlation plot shows the global parameter posterior probability distributions from the nested sampling analysis. Upper right corner shows physical parameters derived from the fitted parameters. The position of the median of each posterior probability distribution is marked with red grid lines. The black contours on the 2D panels represent the 1σ, 2σ, and 3σ confidence levels of the overall posterior samples. The panels on each diagonal show the 1D histogram distribution of each parameter, while the dashed black lines show the 68.3% percentiles. Numerical results are listed in Table S6.
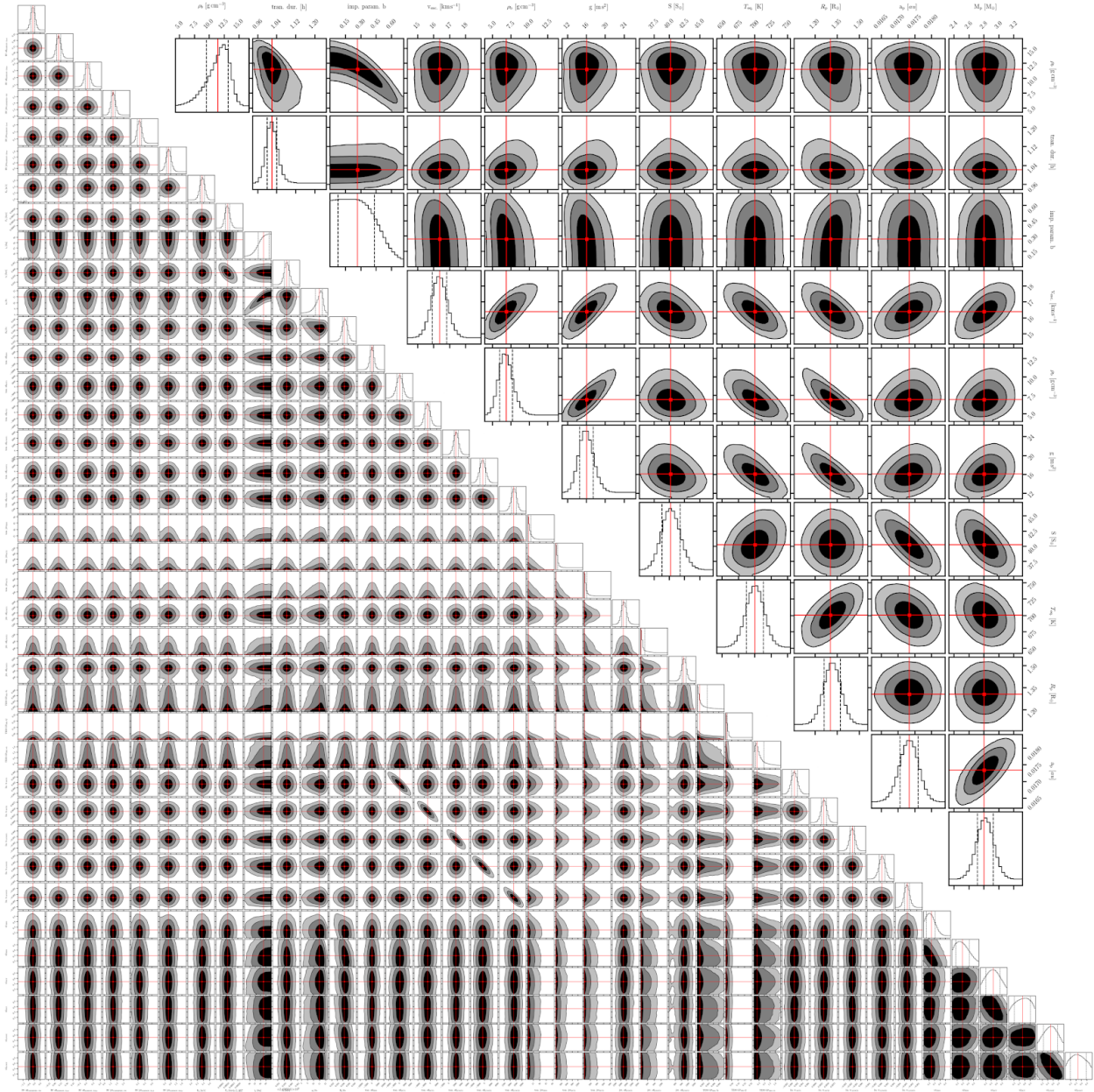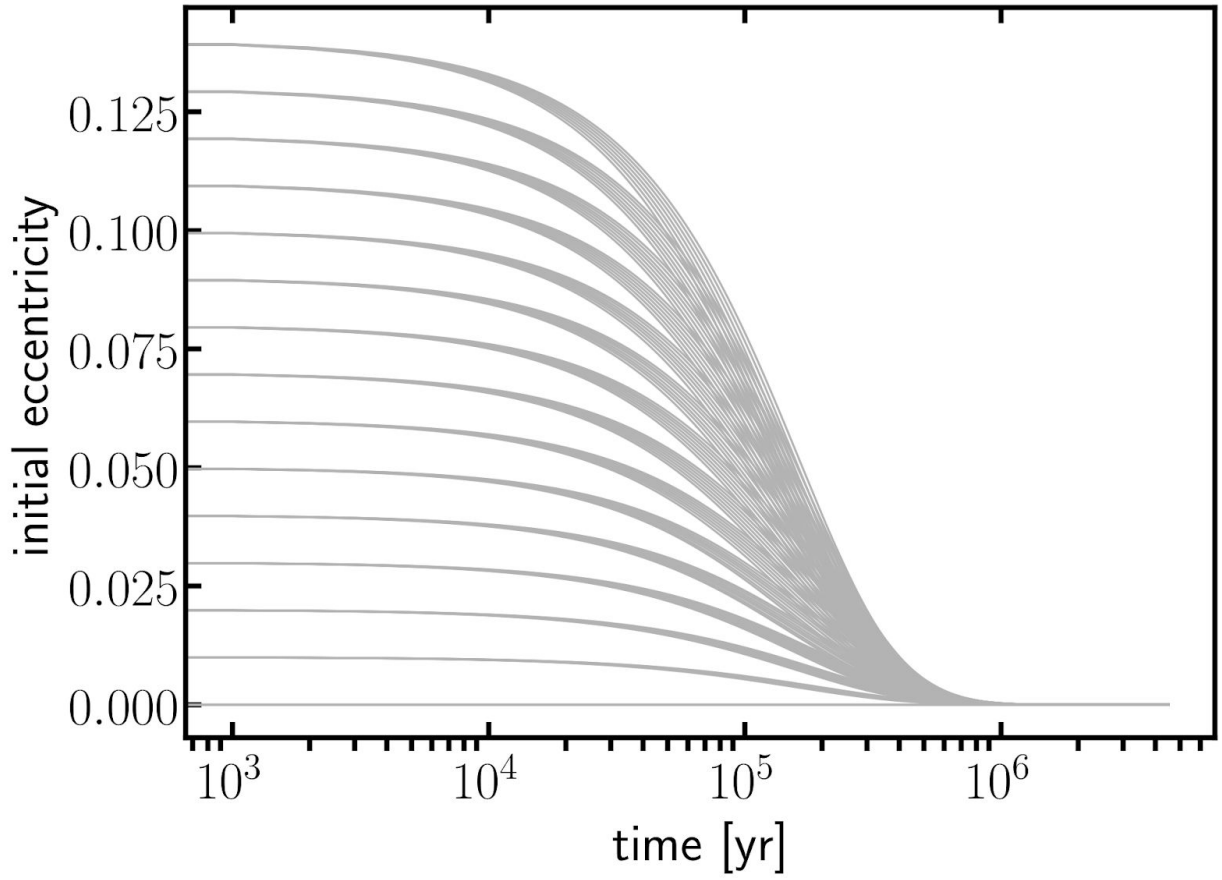
Fig. S9. Same as Fig. S8, but for the CMT+LM model.

Fig. S10. Eccentricity evolution of Gliese 486 achieved via planet-star tidal simulations. The trajectories are constructed for various sets of initial eccentricities and semi-major axes near the best-fit of Gliese 486 b. All eccentricity trajectories converge to a circular orbit within one million year.